


## RESEARCH ARTICLE

# Identifying the crystal and electronic structure evolution in tri-component transition metal oxide nanosheets for efficient electrocatalytic oxygen evolution

Xiaoping Zhang<sup>1</sup> | Chung-Li Dong<sup>2</sup> | Zhidan Diao<sup>1</sup> | Ying-Rui Lu<sup>2,3</sup> | Shaohua Shen<sup>1</sup> 

<sup>1</sup>International Research Center for Renewable Energy, State Key Laboratory of Multiphase, Flow in Power Engineering, Xi'an Jiaotong University, Xi'an, Shaanxi, China

<sup>2</sup>Department of Physics, Tamkang University, New Taipei City, Taiwan

<sup>3</sup>National Synchrotron Radiation Research Center, Hsinchu, Taiwan

## Correspondence

Shaohua Shen, International Research Center for Renewable Energy, State Key Laboratory of Multiphase, Flow in Power Engineering, Xi'an Jiaotong University, Xi'an, Shaanxi 710049, China.  
Email: shshen\_xjtu@mail.xjtu.edu.cn

## Funding information

National Natural Science Foundation of China, Grant/Award Numbers: 51961165103, 51672210; National Program for Support of Top-notch Young Professionals

## Abstract

Transition metal oxides (TMOs) nanosheets comprised of earth abundant Fe, Co, and Ni elements have been designed. Remarkably, the tri-component NiCoFeO<sub>x</sub>/Ni foam (NF) electrode delivers a high current density of 100 mA cm<sup>-2</sup> at an overpotential of only ≈383 mV for oxygen evolution reaction (OER), with prolonged electrochemical stability. The improved OER activity of NiCoFeO<sub>x</sub>/NF can be ascribed to the simultaneous incorporation of Ni and Co into FeO<sub>x</sub>/NF, boosting the intrinsic catalytic activities by altering the crystal and electronic structures. With electron redistribution happening in the tri-component NiCoFeO<sub>x</sub>/NF, the electron transfer from Co to Ni through the Fe acting as the electron transfer bridge renders Co more acidic (Lewis acid) to activate H<sub>2</sub>O (Lewis base) molecules through Lewis acid-base interaction. By identifying the interactions of Fe, Co, and Ni and electron redistribution in the tri-component TMOs, this study provides new insights into the crystal and electronic structure evolution of tri-component NiCoFeO<sub>x</sub> catalysts for active electrocatalysis.

## KEYWORDS

crystal structures, electrocatalytic water splitting, electronic structures, oxygen evolution reaction, transition metal oxides

## 1 | INTRODUCTION

Over the past few years, great efforts have been devoted to the electrochemical study of water splitting for hydrogen and oxygen evolution in pursuit of sustainable and efficient energy conversion and storage.<sup>1</sup> In comparison to hydrogen evolution reaction during water splitting, the oxygen evolution reaction (OER) involves a four-electron process and is more challenging due to its slow reaction kinetics, high overpotentials, and the inferior stability of catalysts.<sup>2-5</sup> Thus,

to enhance the efficiency for electrocatalytic water splitting, suitable and effective electrocatalysts have been explored to trim down the anodic overpotential and to enhance the activity for OER. To date, iridium (Ir) and ruthenium (Ru) oxides have shown effective OER catalytic activities in aqueous media. However, the practical applications of IrO<sub>x</sub> and RuO<sub>x</sub> are limited by their scarce availability and high cost.<sup>6-8</sup> To this end, non-precious metal oxides based on first-row transition metals those are naturally abundant, comparable activity and stability have appeared at

This is an open access article under the terms of the Creative Commons Attribution License, which permits use, distribution and reproduction in any medium, provided the original work is properly cited.

© 2019 The Authors. *EcoMat* published by John Wiley & Sons Australia, Ltd on behalf of The Hong Kong Polytechnic University

the forefront of electrocatalyst research.<sup>9-12</sup> In addition, they exhibit rich chemistries, such as variable oxidation states and advantaged phase changes during the electrochemical processes, which can be also easily tuned and synthesized at large scale for targeted applications.<sup>13-16</sup>

Recently, extensive research efforts have been focused on the transition metal oxides (TMOs), especially, those Fe, Co, and Ni-based oxides, with large surface area, plenty of active sites by tuning the morphology and structure, which aims to boost the inward diffusion of electrolyte ions and improve the intrinsic electrochemical performance. For example, rod-like, mixed rod-like and sheet-like, and sheet-like  $\text{Co}_3\text{O}_4$  nanostructures were prepared by Zhang et al for efficient OER,<sup>17</sup> and  $\text{Co}_3\text{O}_4$  nanosheets exhibited the highest current density and lowest overpotential, which can be attribute to its short electrolyte infiltration diffusion path lengths and low charge transfer resistance. Han and co-workers reported that Ni-Co Prussian-blue-analog (PBA) nanocages exhibited a small overpotential of 380 mV to generate a current density of  $10 \text{ mA cm}^{-2}$ .<sup>18</sup> The outstanding electrocatalytic activity of Ni-Co PBA nanocages came from their complex three-dimensional (3D) cage-like hollow and porous structure. Wang's group reported that ultrathin CoFe layered double hydroxides nanosheets exhibited a low overpotential of 266 mV at  $10 \text{ mA cm}^{-2}$  for efficient OER,<sup>19</sup> which was ascribed to a great number of active sites and vacancies. Tri-component NiCoFe-based catalysts have also aroused much attention, given the abundant high-valence species for enhancing the electrophilicity of the adsorbed O, and thus facilitating the reaction of an  $\text{OH}^-$  anion with an O atom adsorbed at the catalytic active sites to form adsorbed  $-\text{OOH}$ . Qian et al. discovered that the trimetallic NiCoFe-based MOF nanofoam obtained by a facile ambient temperature solution phase method delivered high OER activity,<sup>20</sup> due to the metal hydroxide and oxyhydroxide evolved during electrocatalysis acting as the active species, with morphology and composition optimized from the hierarchical foam-like MOF architecture. Using a rapid modified bluing treatment approach, Xie et al. discovered that a ternary NiCoFe spinel oxide catalyst achieved highly efficient OER performance,<sup>21</sup> which can be attributed to the synergy of multielements, the enriched high-valence species and good structural stability. All these examples showed that TMOs could be recognized as an emerging family of efficient electrocatalysts for OER, owing to the most-optimal M-O bond strength with the formed M-OH, M-O, M-OOH, and M-OO bonds acting as electrocatalytically active intermediates for OER.<sup>22-25</sup>

To further unravel the fundamentals of catalytic mechanisms and then provide guidable principles of designing catalysts for OER, increasing research studies have been focused on the identification of the structure evolution of active phases and the interactions of metal cations in TMOs, especially for some bicomponent (ie, NiFe, NiCo) metal oxides,

during OER processes.<sup>26-29</sup> Friebe et al. elucidated that the active sites of Fe cations in  $\text{Ni}_{1-x}\text{Fe}_x\text{OOH}$  presented the altered electronic properties, resulting in the dramatically changed chemical bonding of Ni and Fe cations with  $\gamma\text{-NiOOH}$  intermediates involved in OER, which gave rise to a lower overpotential and then the improved electrocatalytic activity.<sup>30</sup> Li et al. speculated that the  $\text{Fe}^{3+}$  doping promoted the formation of  $\text{Ni}^{4+}$  in Fe-doped Ni oxides, in which the  $\text{Ni}^{4+}$  species directly contributed to the enhanced OER activity with  $\text{Ni}^{4+}$ -containing  $\gamma\text{-NiOOH}$  phase formed during OER reaction.<sup>31</sup> Using Operando Raman spectroscopy and electrochemical techniques, Chen et al. identified the formation of a unique OER-active structure for  $\text{NiCoO}_x\text{H}_y$  catalysts, in which the catalyst transformed from spinel to amorphous  $\alpha\text{-CoO}$  and then to the OER-active structure  $\text{NiOOH-}h\text{-CoO}_2$  at 0.2 and 0.3 V vs Ag/AgCl, respectively.<sup>32</sup>

All these observations demonstrate that it is of great concern to optimize the crystal and electronic structures, by identifying the interactions of metal cations in TMOs, especially those multi-component metal oxides, for the design of high efficiency electrocatalysts for OER. As discussed above, although many research works have been focused on the NiCoFe-based catalysts, the optimization of the crystal and electronic structures by identifying the interactions of Fe, Co, and Ni and the electron redistribution in tri-component TMOs is still rarely reported.

With keeping aiming at those generally used transition metals (TM = Fe, Co, and Ni) for electrocatalysis, herein, TMOs nanosheets were directly grown on Ni foam (NF) substrates through a facile hydrothermal route followed by thermal treatment. The 3D interconnected macroscopic porous structure across the whole NF substrate not only enables the interior area to be accessible for deposition of catalysts, but also facilitates the mass transport of the reactant hydroxide ions and fast dissipation of gaseous products (eg,  $\text{O}_2$  for OER reaction). It was demonstrated that among the single-metal-component TMOs/NF (TMOs =  $\text{FeO}_x$ ,  $\text{CoO}_x$ ,  $\text{NiO}_x$ ),  $\text{FeO}_x/\text{NF}$  was most catalytically effective in the electrochemical behavior for OER. In order to enhance the catalytic performance of  $\text{FeO}_x/\text{NF}$ , Co and/or Ni were introduced into  $\text{FeO}_x/\text{NF}$  to obtain bi-component ( $\text{NiFeO}_x/\text{NF}$ ,  $\text{CoFeO}_x/\text{NF}$ ) and tri-component ( $\text{NiCoFeO}_x/\text{NF}$ ) metal oxides. In comparison to the separate introduction of Ni or Co into  $\text{FeO}_x/\text{NF}$  yielding no enhancement in electrocatalytic activity and even poorer activity than  $\text{FeO}_x/\text{NF}$ , it is surprising that with Ni and Co simultaneously introduced into  $\text{FeO}_x/\text{NF}$ , the obtained tri-component  $\text{NiCoFeO}_x/\text{NF}$  performed as an outstanding OER catalyst, achieving a high current density of  $100 \text{ mA cm}^{-2}$  at an overpotential of 383 mV and low Tafel slope of  $44.7 \text{ mV dec}^{-1}$ . The greatly improved OER activity of  $\text{NiCoFeO}_x/\text{NF}$  as compared with other TMOs/NF ( $\text{NiO}_x/\text{NF}$ ,  $\text{CoO}_x/\text{NF}$ ,  $\text{FeO}_x/\text{NF}$ ,

NiFeO<sub>x</sub>/NF, CoFeO<sub>x</sub>/NF) can be ascribed to the synergistic evolution of crystal structures (from single crystalline to polycrystalline) and electronic structures, with the simultaneous incorporation of Ni and Co into FeO<sub>x</sub>/NF. It was revealed that in the tri-component NiCoFeO<sub>x</sub>/NF, the introduced Co cations tended to substitute at the Fe sites along with Fe vacancies created, while the introduced Ni cations existed as NiO<sub>x</sub>. With electron redistribution happening along with the crystal structure evolution, Fe served as the electron transfer bridge, promoting the charge transfer from Co to Ni, which renders Co more acidic (Lewis acid) to activate H<sub>2</sub>O (Lewis base) molecules through Lewis acid-base interaction. Therefore, tuning the crystal and electronic structures by tailoring the chemical compositions of transition-metal based materials with the introduction of suitable cations emerges as an effective approach to achieve outstanding electrocatalytic performances for water splitting.

## 2 | RESULTS AND DISCUSSION

These nanostructured TMOs/NF electrodes were successfully prepared by a simple hydrothermal process as schemed in Figure 1A. TMOs nanosheets were directly

grown on NF substrates in aqueous solution containing metal nitrates in stoichiometric ratios, followed by an annealing process. Figure 1B-G displays the SEM images of the NF substrates hydrothermally deposited with TMOs nanosheets. It can be observed that the TMOs nanosheets grow on the skeletons of the NF with uniform morphology, forming a 3D network with highly open structure. Clearly, the NiO<sub>x</sub>/NF and CoO<sub>x</sub>/NF (Figure 1B,C) nanosheets are of multilayered structure with thickness varying from 50 to 100 nm. In comparison, with the introduction of Fe, all the Fe-contained TMOs (Figure 1D-G) nanosheets show an obvious decrease in thickness. Especially, the NiCoFeO<sub>x</sub> nanosheets grown on NF (Figure 1G) display the nanosheet thickness greatly reduced to be several nanometers and the two-dimensional nanosheet size much increased to be several micrometers, as compared with other TMOs. Due to the low loading contents of TMOs ( $\approx 0.1 \text{ mg cm}^{-2}$ ), all the TMOs/NF electrodes exhibit three distinct diffraction peaks of NF substrates at 44.5°, 51.8°, and 76.4° (PDF#65-2865),<sup>33</sup> without any other peaks observed in the X-ray diffraction (XRD) patterns (Figure S1, Supporting Information). However, all the precipitates, collected after hydrothermal process and undergone an annealing process similar to TMOs/NF, exhibit diffraction peaks at around 35.6°, 43.3°, and 62.9° (Figure S2,

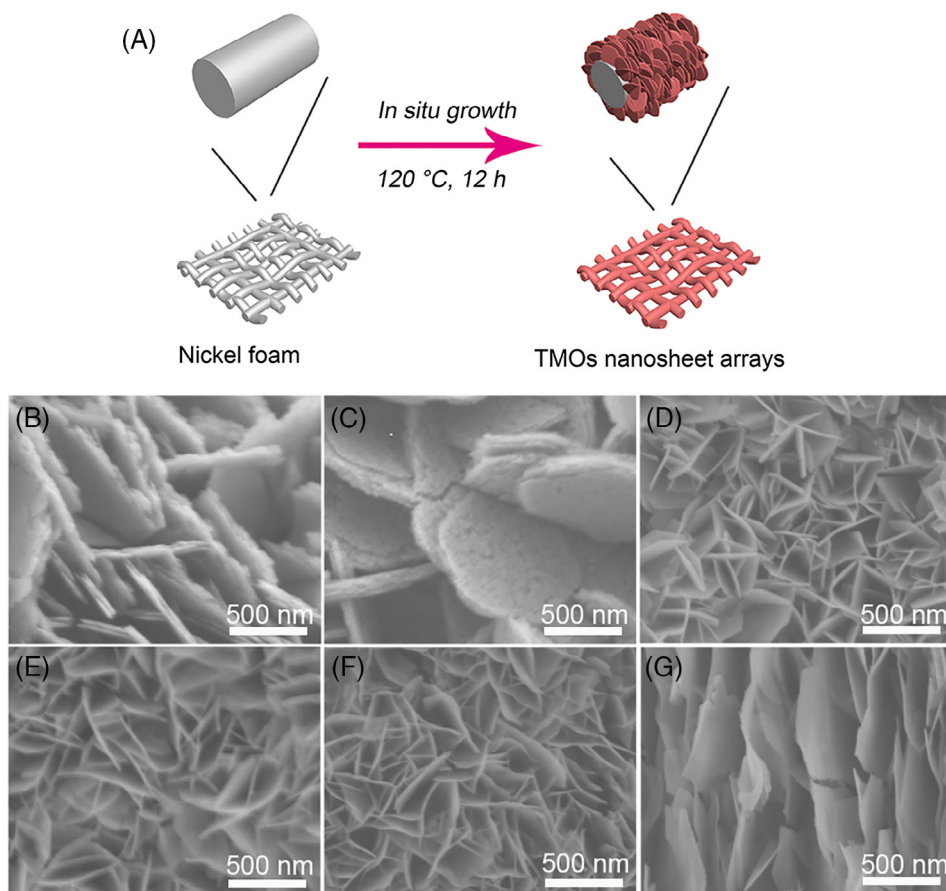


**FIGURE 1** A, Schematic illustration of the transition metal oxides (TMOs) nanosheets grown on Ni foam (NF) via a hydrothermal method, SEM images of: B, NiO<sub>x</sub>/NF; C, CoO<sub>x</sub>/NF; D, FeO<sub>x</sub>/NF; E, NiFeO<sub>x</sub>/NF; F, CoFeO<sub>x</sub>/NF; and G, NiCoFeO<sub>x</sub>/NF

Supporting Information), which is consistent with the standard pattern of  $\text{FeO}_x$  (PDF#39-1346).<sup>34</sup> This indicates that all the hydrothermally grown TMOs have similar crystal structure.

Given the fact that  $\text{FeO}_x/\text{NF}$  was measured to have the highest electrocatalytic OER activity among the three single-component TMOs/NF electrodes (see the electrochemical measurements in the following sections), the discussion and analysis on crystal structure and electronic structure as well as the electrocatalytic activity of the bicomponent and tri-component TMOs/NF electrodes in the following sections was carried out with the  $\text{FeO}_x/\text{NF}$  electrode as reference.

More details in the structural and morphological features of the prepared TMOs nanosheets were further investigated by transmission electron microscopy (TEM) images. As shown in Figure 2A, the semi-transparent  $\text{FeO}_x$  nanosheets indicate the very thin thickness of the single layer, which is determined to be only  $\approx 4.5$  nm. In comparison, the TMOs containing two metallic elements (ie,  $\text{NiFeO}_x$ ,  $\text{CoFeO}_x$ ) display even smaller single-layer thickness of  $\approx 4.0$  nm for  $\text{NiFeO}_x$  and  $\approx 3.5$  nm for  $\text{CoFeO}_x$  (insets in Figure 2B,C), with the second transition metal

introduced. Especially, the ternary  $\text{NiCoFeO}_x$  shows the smallest single-layer thickness of only  $\approx 2.5$  nm (inset in Figure 2D). Furthermore, the ultrathin feature of the nanosheets is also confirmed by atomic force microscopy (AFM). It can be found that the as-prepared nanosheets have thickness of 4.0 to 4.5 nm, 3.5 to 4.0 nm, 3.0 to 3.5 nm, and 2.0 to 3.0 nm for  $\text{FeO}_x$ ,  $\text{NiFeO}_x$ ,  $\text{CoFeO}_x$ , and  $\text{NiCoFeO}_x$  (Figure S3, Supporting Information), respectively, which are consistent with the thickness in the TEM images. As shown in the high-resolution TEM image (Figure 2E), the lattice spacings of 0.24 nm can be well assigned to the (311) planes of  $\text{FeO}_x$ ,<sup>35</sup> and  $\text{FeO}_x$  nanosheets demonstrate the single-crystalline nature (inset in Figure 2E) of well-defined and continuous crystal lattice with defects hardly observed. However, with the second transition metal Ni or Co introduced into the  $\text{FeO}_x$  nanosheets homogeneously (Figure S4, Supporting Information), the lattice spacings of the obtained binary  $\text{NiFeO}_x$  and  $\text{CoFeO}_x$  decrease to 0.22 and 0.21 nm, respectively, maybe due to the smaller sizes of Ni and Co ions than Fe ions. Instead of single-crystalline observed for  $\text{FeO}_x$ ,  $\text{NiFeO}_x$ , and  $\text{CoFeO}_x$  display the polycrystalline nature (inset in Figure 2F,G) with defects created. Moreover, the

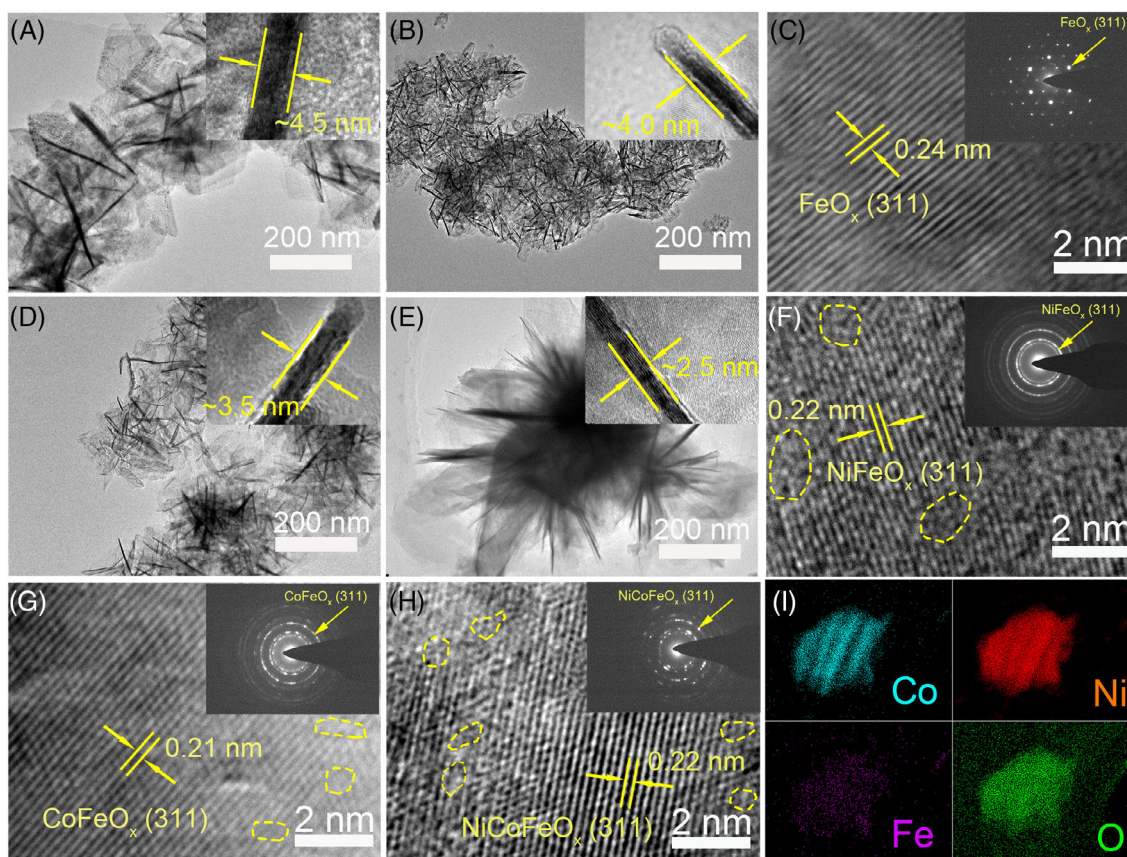


**FIGURE 2** TEM images of: A,  $\text{FeO}_x$ ; B,  $\text{NiFeO}_x$ ; C,  $\text{CoFeO}_x$ ; and D,  $\text{NiCoFeO}_x$ , the insets of, A–D, show the thickness of the nanosheets, and high-resolution transmission electron microscopy images and selected area electron diffraction patterns (inset) of: E,  $\text{FeO}_x$ ; F,  $\text{NiFeO}_x$ ; G,  $\text{CoFeO}_x$ ; H,  $\text{NiCoFeO}_x$ ; and I, elemental mapping of  $\text{NiCoFeO}_x$

introduction of Ni could induce more defects in  $\text{NiFeO}_x$  as than Co in  $\text{CoFeO}_x$  (as marked by the yellow-line circles in Figure 2F,G). With both Ni and Co introduced into  $\text{FeO}_x$  nanosheets, the lattice spacing of the obtained ternary  $\text{NiCoFeO}_x$  reduces to 0.22 nm, and  $\text{NiCoFeO}_x$  also shows the poly-crystalline nature (inset in Figure 2H), with plenty of defects created. The reduction of lattice spacings indicates that the incorporation of Ni and/or Co may trigger crystal structure evolution of TMOs, possibly due to the different sizes of transition metal ions. The scanning EDX elemental mapping (Figure 2I and Figure S4 in Supporting Information) reveals the homogeneous distribution of transition metals in these TMOs nanosheets hydrothermally grown on NF substrates. Thus, it could be deduced that the incorporation of Ni and/or Co could greatly alter the crystal structure of the obtained TMOs nanosheets, with crystal phases transformed from single crystalline for  $\text{FeO}_x$  to poly-crystalline for alloy-based TMOs (ie,  $\text{NiFeO}_x$ ,  $\text{CoFeO}_x$ , and  $\text{NiCoFeO}_x$ ) with defects simultaneously introduced.

X-ray photoelectron spectra (XPS) were collected to reveal the atomic compositions and the chemical states of the as-prepared TMOs nanosheets. Figure 3A shows the Fe 2p spectra of all samples. For  $\text{FeO}_x$ , two peaks with binding energies of Fe 2p<sub>3/2</sub> at 711.3 eV and Fe 2p<sub>1/2</sub> at 724.6 eV could confirm the oxidation state of Fe<sup>3+</sup>.<sup>6,36,37</sup>

With Ni (or Co) introduced into  $\text{FeO}_x$ , both the Fe 2p<sub>3/2</sub> and Fe 2p<sub>1/2</sub> peaks shift to higher (or lower) binding energies for the obtained  $\text{NiFeO}_x$  (or  $\text{CoFeO}_x$ ), indicating that the introduction of Ni or Co atoms into the  $\text{FeO}_x$  lattice may trigger the charge redistribution around the Fe atoms, but in different ways. Then, it is reasonable that with the simultaneous incorporation of Ni and Co atoms into  $\text{FeO}_x$ , the obtained  $\text{NiCoFeO}_x$  shows the Fe 2p<sub>3/2</sub> and Fe 2p<sub>1/2</sub> peaks located between those of  $\text{NiFeO}_x$  and  $\text{CoFeO}_x$ . As shown in Figure 3B, the Ni peaks corresponding to Ni<sup>2+</sup> and Ni<sup>3+</sup> are observed for all the Ni contained TMOs nanosheets. Specifically, the two fitting peaks at 872.0 and 854.6 eV could be ascribed to Ni<sup>2+</sup>, while the two peaks at 873.8 and 855.8 eV should be ascribed to Ni<sup>3+</sup>.<sup>38,39</sup> Similarly, the Co 2p peaks could also be deconvoluted into multi-valence states, for example, Co<sup>2+</sup> with binding energies at 781.2 and 796.9 eV and Co<sup>3+</sup> with binding energies at 779.7 and 795.2 eV (Figure 3C).<sup>40,41</sup> It could be then reasonably expected that the introduction of the redox couples of Ni<sup>2+</sup>/Ni<sup>3+</sup> and Co<sup>2+</sup>/Co<sup>3+</sup> in TMOs nanosheets might alter the charge distribution around the Fe atoms and thus the electronic structure evolution might contribute to the improved electrochemical performances.<sup>42-44</sup> Figure 3D shows the O 1s spectra of all the TMOs/NF samples. For the single metallic TMO sample, that is,  $\text{FeO}_x$ , the peak with a low

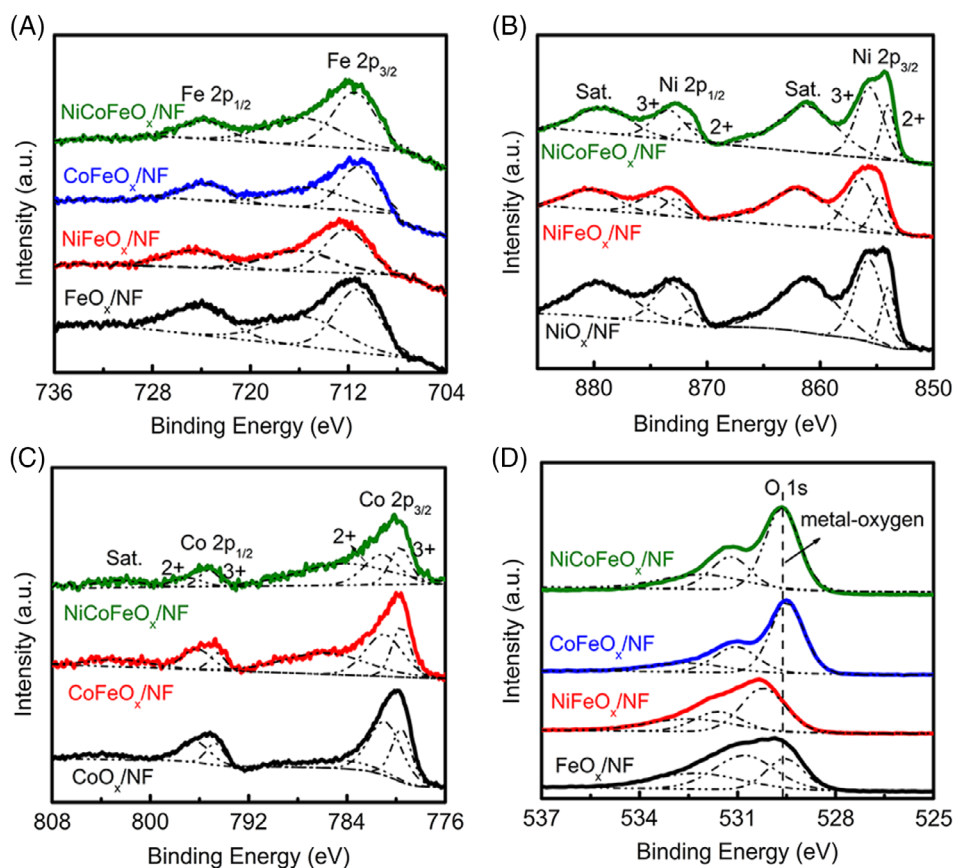


**FIGURE 3** XPS spectra of: A, Fe 2p; B, Ni 2p; C, Co 2p; and D, O 1s for  $\text{NiO}_x/\text{NF}$ ,  $\text{CoO}_x/\text{NF}$ ,  $\text{FeO}_x/\text{NF}$ ,  $\text{NiFeO}_x/\text{NF}$ ,  $\text{CoFeO}_x/\text{NF}$ , and  $\text{NiCoFeO}_x/\text{NF}$

binding energy at 529.6 eV could be assigned to the oxygen–metal bond (Fe–O).<sup>45,46</sup> The second peak at 531.0 eV should be attributed to the defects with low oxygen coordination in the materials such as hydroxyls, chemisorbed oxygen and undercoordinated lattice oxygen.<sup>47</sup> The third peak with a higher binding energy at 532.8 eV could be attributed to the physically and chemically adsorbed water molecules on the surface.<sup>48</sup> Clearly, with Co and/or Ni atoms introduced into FeO<sub>x</sub>, the metal–oxygen (M–O) peaks shift to higher and lower binding energy for the bicomponent NiFeO<sub>x</sub> and CoFeO<sub>x</sub>, respectively, while the tri-component NiCoFeO<sub>x</sub> shows the M–O peak locating between those of NiFeO<sub>x</sub> and CoFeO<sub>x</sub>. This phenomenon is consistent with the binding energy shift of the Fe peaks in these alloy-based TMOs, which again evidences that the introduction of Ni and/or

Co in TMOs nanosheets might alter the charge distribution of the Fe–O bonds. Based on the TEM images and XPS analysis, it could be verified that the introduction of Ni and/or Co into FeO<sub>x</sub> will affect the crystal structures (ie, from single crystalline to poly-crystalline with the introduction of defects) as well as the electronic structures, which in turn would be expected to tune the catalytic activity of these TMOs electrocatalysts.

It is believed that the electrocatalytic activity is strongly associated with the electronic structure. Thus, it would be of great importance to reveal the effect of the incorporated Co and/or Ni on the electronic structures of TMOs nanosheets in more details, by carrying out the X-ray absorption near edge structure (XANES) and extended X-ray absorption fine structure (EXAFS) spectra. Figure 4A shows the Fe K-edge XANES of FeO<sub>x</sub>/NF,

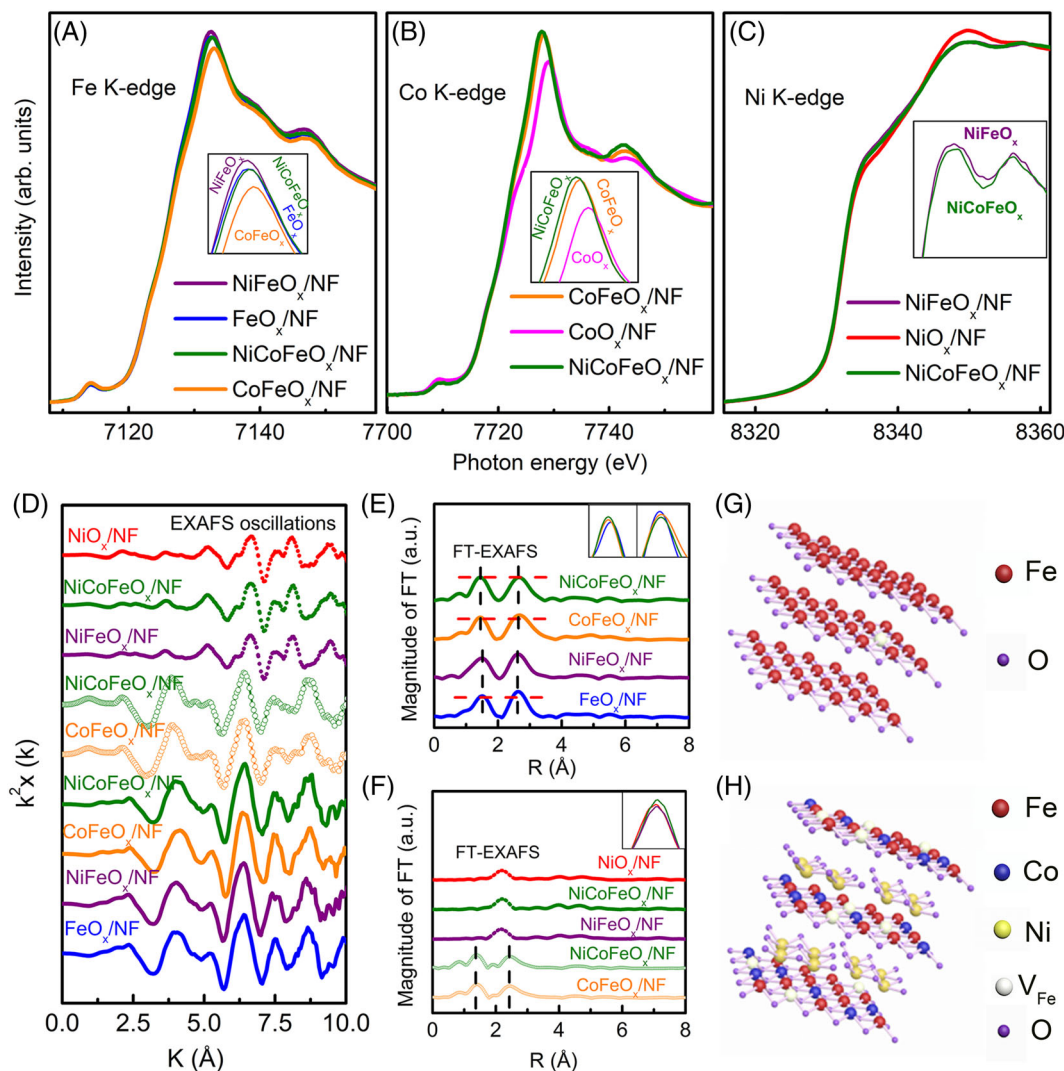


**FIGURE 4** A, Fe K-edge; B, Co K-edge; and C, Ni K-edge XANES spectra; D, extended X-ray absorption fine structure (EXAFS) oscillations of Fe K-edge (solid lines), Co K-edge (line with open circles), and Ni K-edge (dot lines)  $k^2x$  spectra; the Fourier transformed amplitude of the EXAFS  $k^2$  data at the, E, Fe K-edge; F, Co K-edge (open circles), and Ni K-edge (dot lines); schematic representations of the model structures for G, FeO<sub>x</sub>/Ni foam (NF) and H, NiCoFeO<sub>x</sub>/NF

NiFeO<sub>x</sub>/NF, CoFeO<sub>x</sub>/NF, and NiCoFeO<sub>x</sub>/NF. The transition metal K-edge is resulted from the electron transition from 1s core level to 4p unoccupied orbitals. The intensity of the absorption peak is proportion to the amount of unoccupied electronic states. Notably, the peak intensity of Fe K-edge of bi-component CoFeO<sub>x</sub>/NF (NiFeO<sub>x</sub>/NF) is lower (higher) than that of FeO<sub>x</sub>/NF, which implies that there is a charge redistribution upon the incorporation of Co or Ni. For CoFeO<sub>x</sub>/NF, the charge redistribution is likely to be originated from the charge transfer from Co to Fe, which is evidenced by the fact that the peak intensity of Co K-edge (Figure 4B) for CoFeO<sub>x</sub>/NF is higher than that for CoO<sub>x</sub>/NF. Comparatively, with Ni incorporated into FeO<sub>x</sub>/NF, the Fe K-edge of the obtained NiFeO<sub>x</sub>/NF is higher than that of FeO<sub>x</sub>/NF, and main peak of Ni K-edge (Figure 4C) is lower in NiFeO<sub>x</sub>/NF than in NiO<sub>x</sub>/NF, which strongly suggests the Fe and Ni, respectively, loses and gains some charges. Interestingly, as both Co and Ni are incorporated in FeO<sub>x</sub>/NF, the peak intensity of Fe K-edge of the tri-component NiCoFeO<sub>x</sub>/NF is almost identical to that of FeO<sub>x</sub>/NF. This fact along with the analytical results above suggests the charge transfer is from Co to Ni in NiCoFeO<sub>x</sub>/NF, and Fe acts as the electron transfer bridge. To confirm this argument, the Co K-edge (Figure 4B, inset) of CoFeO<sub>x</sub>/NF and NiCoFeO<sub>x</sub>/NF, and Ni K-edge (Figure 4C, inset) of NiFeO<sub>x</sub>/NF and NiCoFeO<sub>x</sub>/NF are compared. NiCoFeO<sub>x</sub>/NF exhibits the higher (lower) peak intensity of Co K-edge (Ni K-edge) than CoFeO<sub>x</sub>/NF (NiFeO<sub>x</sub>/NF). Therefore, Ni gains charges as Co is presented in NiFeO<sub>x</sub>/NF, while Co loses charges as Ni is presented in CoFeO<sub>x</sub>/NF.

Figure 4D presents the EXAFS oscillations of Fe K-edge (solid lines), Co K-edge (line with open circles), and Ni K-edge (dot lines)  $k^2x$  spectra. It is clear that Fe K-edge EXAFS oscillations of NiFeO<sub>x</sub>/NF, CoFeO<sub>x</sub>/NF, and NiCoFeO<sub>x</sub>/NF are similar to each other and resemble that of FeO<sub>x</sub>/NF. This indicates all samples have similar atomic structure around Fe site as compared to FeO<sub>x</sub>/NF. Notably, Co K-edge EXAFS oscillations of CoFeO<sub>x</sub>/NF and NiCoFeO<sub>x</sub>/NF are almost identical and analogous to the Fe K-edge EXAFS oscillations. However, Ni K-edge EXAFS oscillations of the Ni contained TMOs samples closely resemble each other, but differ from Fe K- and Co K-edge EXAFS oscillations. Thus, the atomic structure around Fe and Co sites are alike, but atomic structure around Ni site bears resemblance to NiO<sub>x</sub>/NF. Figure 4E presents the Fourier-transformed (FT) amplitude of the EXAFS  $k^2$  data at the Fe K-edge. The peaks at about 1.5 and 2.5 Å are, respectively, associated with the first coordination shell Fe—O and second coordination shell Fe—Metal (*M*) (*M* = Fe, Co, Ni). Yet again, all samples exhibit the similar coordination shells. Figure 4F shows the FT

EXAFS  $k^2$  signal at the Co K-edge (open circles) and Ni K-edge (dot lines). At a glance, the coordination shells revealed from Co K-edge are different from Ni K-edge but analogous to Fe K-edge. Thus, it could be suggested that Fe and Co locate at similar sites in the crystal lattice, but Ni locates at the position that is different from Co and Fe. Quantitatively, the FT-EXAFS curve-fitted results are shown in Figure S5 (Supporting Information), indicating that the fitting curves are well consistent with the experimental data. The results of the best fits are listed in Tables S1 to S3 (Supporting Information). Notably, the bond length (M—O and M—M) of FeO<sub>x</sub>/NF and NiFeO<sub>x</sub>/NF are almost the same, as indicated by the vertical lines in Figure 4E, suggesting the incorporation of Ni in FeO<sub>x</sub>/NF does not change the bond length and Ni does not replace Fe/Co. The CoFeO<sub>x</sub>/NF and NiCoFeO<sub>x</sub>/NF in Figure 4F can be interpreted along the same lines. Above results suggest that the Co incorporated in FeO<sub>x</sub>/NF is likely to replaces Fe, while the Ni incorporated in FeO<sub>x</sub>/NF appears to be positioned at interstitial site, which would form the local NiO<sub>x</sub>-like atomic environment and create defects in the nanosheets, as clearly observed in TEM images (Figure 2F-H).

Taking a closer look at the FT of EXAFS at Fe K-edge (Figure 4E), in comparison with FeO<sub>x</sub>/NF and NiFeO<sub>x</sub>/NF, the M—O bond length decreases and the M—M bond length increases for CoFeO<sub>x</sub>/NF (1.92 Å) and NiCoFeO<sub>x</sub>/NF (1.91 Å) with Co incorporated, as indicated by two vertical lines in Figure 4E. Furthermore, in presence of Co, the coordination number of M—O (M—M) shell for CoFeO<sub>x</sub>/NF or NiCoFeO<sub>x</sub>/NF is increased (decreased) in comparison with FeO<sub>x</sub>/NF, as indicated by the horizontal red lines revealing the ratio of FT-EXAFS intensity of M—O to M—M shell is lowest for FeO<sub>x</sub>/NF. The detailed variation of coordination numbers for M—O and M—M shell is depicted in Table S1 (Supporting Information). The enlarged coordination number in first M—O shell and the shrunken M—O bond length, together with the reduced coordination number in second M—M shell and increased M—M bond length, reveal that Co tends to substitute Fe. However, some Fe is not replaced successfully by Co, thus generating the Fe vacancies. By comparing NiFeO<sub>x</sub>/NF and FeO<sub>x</sub>/NF, the change of M—O and M—M coordination number and bond length is insignificant, which suggests the effects of Ni incorporated in FeO<sub>x</sub> are different from that of Co incorporated, and there is no substitution effect when Ni is incorporated. These observations may explain why the single-crystal like FeO<sub>x</sub> no longer persists as Co and/or Ni are introduced, and instead poly-crystalline with defects introduced is formed. This phenomenon is also verified in the identical FT of EXAFS at Co K-edge for CoFeO<sub>x</sub>/NF and NiCoFeO<sub>x</sub>/NF, as shown in Figure 4F. The FT-EXAFS

curve fitting of Co K-edge is displayed in Figure S5C with the best fits listed in Table S2 (Supporting Information). The difference in the coordination number and bond length can be hardly observed. Thus, the presence of NiO<sub>x</sub> has nearly no influence on the atomic structures around Fe and Co sites in these samples. To further address the effect of NiO<sub>x</sub> in bi-component or tri-component samples, the FT of EXAFS at Ni K-edge for NiFeO<sub>x</sub>/NF, NiCoFeO<sub>x</sub>/NF, and NiO<sub>x</sub>/NF are compared (Figure 4F). The tri-component sample exhibits the largest peak intensity in comparison with single- and bi-component samples, implying that the Ni–O coordination number is highest in NiCoFeO<sub>x</sub>/NF, which is evidenced in the best fits in Table S3 (Supporting Information). The enhanced Ni–O coordination number may play an important role to connect the CoFeO<sub>x</sub>/NF fragments to

form poly-crystalline NiCoFeO<sub>x</sub>/NF. Based on these X-ray absorption spectroscopy (XAS) results, as proposed in the model structures (Figure 4G,H), the introduced Co tends to substitute at the Fe sites along with Fe vacancies created, while the introduced Ni tends to exist in NiO<sub>x</sub> form.

The electrochemical measurements were conducted in a typical three-electrode setup in 1.0 M NaOH solution to explore these TMOs/NF electrodes used for OER. Bare NF shows a very poor OER activity, and in comparison, considerable OER activities were observed for NiO<sub>x</sub>/NF, CoO<sub>x</sub>/NF, and FeO<sub>x</sub>/NF (Figure 5A). The overpotential required to drive a current density of 100 mA cm<sup>-2</sup> for OER decreases from 526 mV for NF to 467, 447 and 402 mV for NiO<sub>x</sub>/NF, CoO<sub>x</sub>/NF, and FeO<sub>x</sub>/NF, respectively. To ascertain the reaction kinetics, Tafel analysis was conducted (Figure 5B), with Tafel slopes

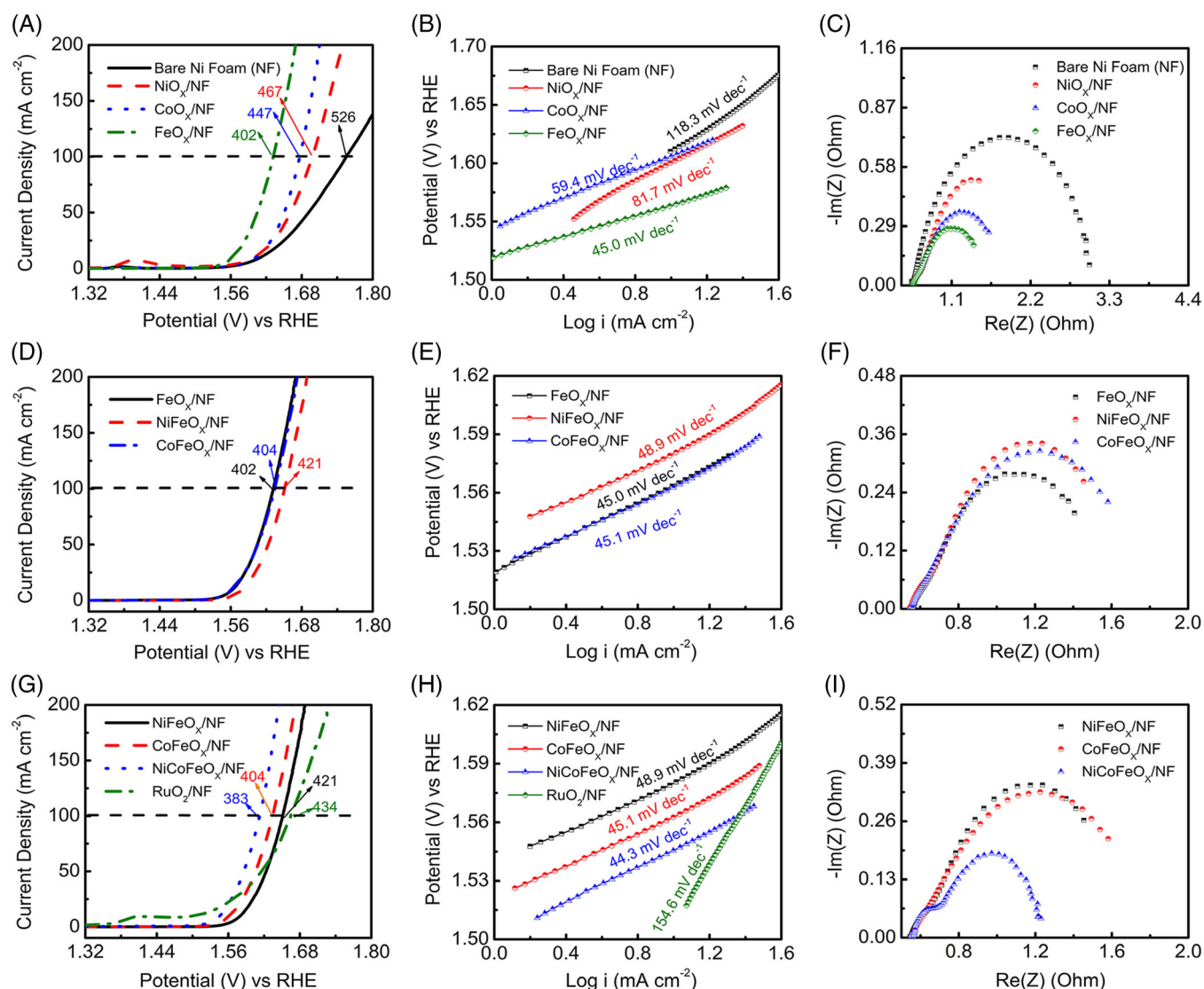


**FIGURE 5** A,D,G, The linear sweep voltammogram (LSV) curves; B,E,H, Tafel plots; and C,F,I, Nyquist plots of transition metal oxides (TMOs)/Ni foam (NF) in 1.0 M NaOH



determined to be 118.3, 81.7, 59.4, and 45.0 mV dec<sup>-1</sup> for bare NF, NiO<sub>x</sub>/NF, CoO<sub>x</sub>/NF, and FeO<sub>x</sub>/NF, respectively. Comparatively, among these single-metal-component TMOs/NF, FeO<sub>x</sub>/NF was the most catalytically effective in the electrochemical behavior for OER.

In order to enhance the electrocatalytic OER performance of FeO<sub>x</sub>/NF, a second metal component (eg, Co and Ni) was introduced into FeO<sub>x</sub>/NF, yielding bi-component NiFeO<sub>x</sub>/NF and CoFeO<sub>x</sub>/NF. However, the overpotentials required to drive a current density of 100 mA cm<sup>-2</sup> for OER are 421 and 404 mV for NiFeO<sub>x</sub>/NF and CoFeO<sub>x</sub>/NF (Figure 5D), respectively, which are even larger than that of FeO<sub>x</sub>/NF. Accordingly, the Tafel slopes were determined to be 48.9 and 45.1 mV dec<sup>-1</sup> for NiFeO<sub>x</sub>/NF and CoFeO<sub>x</sub>/NF (Figure 5E), respectively, larger than that of FeO<sub>x</sub>/NF, which evidences that the incorporation of Co or Ni could hardly enhance the catalytic performance of FeO<sub>x</sub>/NF for OER. Surprisingly, when Co and Ni were simultaneously incorporated into FeO<sub>x</sub>/NF to form tri-component TMOs/NF (see Figure S6 and related discussion), that is, NiCoFeO<sub>x</sub>/NF, the overpotential required to drive a current density of 100 mA cm<sup>-2</sup> for OER was greatly reduced to 383 mV, even smaller than that of RuO<sub>2</sub>/NF as the benchmarking noble-metal electrocatalyst (434 mV at 100 mA cm<sup>-2</sup>), along with a much reduced Tafel slope of 44.7 mV dec<sup>-1</sup> (Figure 5G,H), which implies that the simultaneous incorporation of Ni and Co play a synergistic role in boosting the catalytic activity of FeO<sub>x</sub>/NF for OER. It is then noteworthy that the tri-component NiCoFeO<sub>x</sub>/NF electrocatalyst performs an admirable OER activity in alkaline solution, as compared to other reported electrocatalysts (Table S4, Supporting Information).

To gain further insightful understanding into the improvement in electrochemical performance of the tri-component NiCoFeO<sub>x</sub>/NF electrode, electrochemical impedance spectra (EIS) of all the electrodes were collected (Figure 5C,F,I), with EIS results fitted by equivalent circuit (Figure S7, Supporting Information) and listed in Table S5 (Supporting Information). Here,  $R_s$  is the series resistance, and  $R_{ct}$  ( $R_{ct1}$ ,  $R_{ct2}$ ) represents the charge transfer resistances. In the case of TMOs/NF,  $R_{ct1}$  signifies the resistance of charge transfer from the catalyst to the electrolyte, whereas  $R_{ct2}$  indicates the resistance of charge transfer from the NF to the TMOs catalyst. Though the  $R_{ct1}$  of NiCoFeO<sub>x</sub>/NF electrode (0.181 Ω) is slightly larger than FeO<sub>x</sub>/NF electrode (0.138 Ω), the total resistance ( $R_{ct1} + R_{ct2}$ ) of the NiCoFeO<sub>x</sub>/NF electrode (0.686 Ω) is much smaller than others (1.728 Ω for NiO<sub>x</sub>/NF, 1.321 Ω for CoO<sub>x</sub>/NF, 1.016 Ω for FeO<sub>x</sub>/NF, 1.152 Ω for NiFeO<sub>x</sub>/NF, and 1.242 Ω for CoFeO<sub>x</sub>/NF). The small charge transfer resistance, which benefits the efficient charge transport, is partly due to the simultaneous incorporation of Ni and Co

tuning the electronic structures of NiCoFeO<sub>x</sub>/NF. This result also demonstrates that the synergistic incorporation of Ni and Co gives rise to the promoted catalyst/electrolyte charge transfer processes and the accelerated catalysis kinetics for OER, and thus the improved electrocatalytic activity for water oxidation.<sup>49,50</sup>

In addition, the electrochemically active surface areas (ECSAs) of the as-made FeO<sub>x</sub>/NF, NiFeO<sub>x</sub>/NF, CoFeO<sub>x</sub>/NF, and NiCoFeO<sub>x</sub>/NF were estimated from the electrochemical double-layer capacitance ( $C_{dl}$ ),<sup>51</sup> measured by a series of cyclic voltammetry curves under different scan rates in 1.0 M NaOH (Figure S8, Supporting Information). As shown in Figure S9 (Supporting Information), the NiCoFeO<sub>x</sub>/NF electrode (0.098 F cm<sup>-2</sup>) exhibits  $C_{dl}$  larger than other electrodes (0.084 F cm<sup>-2</sup> for FeO<sub>x</sub>/NF, 0.093 F cm<sup>-2</sup> for NiFeO<sub>x</sub>/NF, and 0.087 F cm<sup>-2</sup> for CoFeO<sub>x</sub>/NF), revealing the increased ECSA with Ni and Co simultaneously introduced into FeO<sub>x</sub>/NF. The increase in ECSA of the NiCoFeO<sub>x</sub>/NF electrode can be attributed to the smaller nanosheet thickness, the introduced Fe vacancies and the crystal structure evolution (ie, from single crystalline to polycrystalline with the introduction of defects), as induced by the simultaneous Ni and Co incorporation, which may provide more exposed active sites for OER.

The long-term durability of electrocatalysts is another crucial factor to be considered for practical applications. As shown in Figure 6A, the NiCoFeO<sub>x</sub>/NF electrode shows a slight decay in current density in the first 6 hours and maintains unchanged with OER prolonging to 12 hours, indicating the good stability of the TMOs/NF electrodes for OER. Further evidentially, after 12 hours long-term measurement, the linear sweep voltammogram (LSV) curve of the NiCoFeO<sub>x</sub>/NF exhibits an onset potential almost the same as that of the initial cycle (inset in Figure 6A). After electrochemical reaction, the layered morphology of NiCoFeO<sub>x</sub>/NF (Figure S11, Supporting Information) is almost the same as those of the original sample (see Figure S10 and related discussion in the Supporting Information), further evidencing the good morphological stability of NiCoFeO<sub>x</sub>/NF for OER. Then, the stability decay in the initial OER period should be due to the etching of the metal elements during the surface phase transformation (see Figure S12 and related discussion in the Supporting Information). It is interestingly observed that, with the chemical states of Fe and Co (Figure S12A,B) maintained unchanged, NiCoFeO<sub>x</sub>/NF after stability test has the higher Ni<sup>3+</sup> content at the surface as compared to original NiCoFeO<sub>x</sub>/NF (Figure S12C), and such change in Ni oxidation states demonstrates the possible formation of oxyhydroxide during water oxidation process.<sup>20</sup> Meanwhile, a slight shift in binding energy could be observed in the O1s spectra (Figure S12D), which

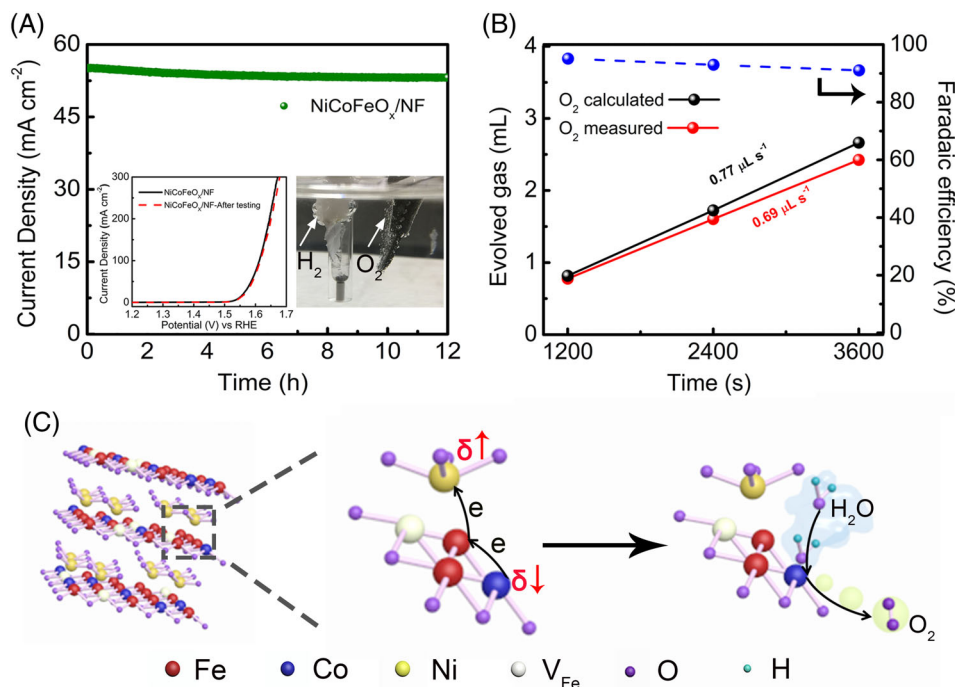


**FIGURE 6** A, Time-dependent current density curves of NiCoFeO<sub>x</sub>/Ni foam (NF) at 1.58 V vs reversible hydrogen electrode (RHE) for 12 hours, in 1.0 M NaOH. B, The measured and calculated amounts of O<sub>2</sub> gas evolved during oxygen evolution reaction (OER) with corresponding Faradaic efficiencies of NiCoFeO<sub>x</sub>/NF. C, The mechanism schematics of the outstanding catalytic activities of NiCoFeO<sub>x</sub>/NF for OER

also indicates the surface phase transformation from metal oxide component to metal hydroxide component during the water oxidation reaction. Similar phenomenon has been well documented in TMOs for OER, and the derived oxide/hydroxide species has been evidenced for the superior catalytic performance toward water oxidation.<sup>32</sup> The amounts of O<sub>2</sub> evolved at NiCoFeO<sub>x</sub>/NF electrode were collected during the chronoamperometry test at 1.54 V vs reversible hydrogen electrode (RHE) to determine the Faradic efficiency. As shown in Figure 6B, the O<sub>2</sub> gas was linearly produced with reaction time prolonging, with the evolution rates of O<sub>2</sub> theoretically calculated and experimentally measured to be 0.77 and 0.69 μL s<sup>-1</sup>, respectively. The calculated Faradaic efficiencies of the evolved O<sub>2</sub> were then determined to be over 90%, meaning that almost all the generated charges were utilized for OER.

As revealed in the above crystal and electronic structural analysis, in the tri-component NiCoFeO<sub>x</sub>/NF, the incorporated Co tends to partially substitute the Fe along with Fe vacancies generated, while the incorporated Ni mainly exists in NiO<sub>x</sub> form. Along with the crystal structure transformation from single to polycrystalline phase, the electronic structure evolution was also monitored and analyzed in XANES and EXAFS spectra. As proposed in Figure 6C, with Co and Ni together introduced into FeO<sub>x</sub>/NF, the electron transfer from Co to Ni happens in the tri-component NiCoFeO<sub>x</sub>/NF, with the Fe acting as the electron transfer bridge. Thus, the charge density of Co decreases (δ<sub>↓</sub>) and the charge density of Ni increases (δ<sub>↑</sub>). This electron donation from Co to Ni will make Co more acidic (Lewis acid), which facilitates the activation

of H<sub>2</sub>O (Lewis base) molecules through Lewis acid-base interaction. It could be then reasonably expected that the strong electron interactions and the charge redistribution between Co, Fe, and Ni in NiCoFeO<sub>x</sub>/NF should be also beneficial to the intrinsic electrochemical performances for OER. In a word, the simultaneous Co and Ni incorporation would trigger crystal structure and electronic structure evolution, synergistically increasing the population and the intrinsic activity of active sites, which should be responsible for the accelerated charge transfer process and the surface catalysis kinetics, and then the excellent performance of the NiCoFeO<sub>x</sub>/NF electrode for OER.

### 3 | CONCLUSION

In summary, nanosheet-like TMOs deposited on 3D conductive nickel foam (NF) substrates were prepared through a cost-effective hydrothermal method. These obtained TMOs nanosheets show excellent OER electrocatalytic performance and durability in alkaline electrolytes. Especially, the tri-component NiCoFeO<sub>x</sub>/NF electrode needs a small overpotential of only about 383 mV to achieve a pretty high current density of 100 mA cm<sup>-2</sup> for OER. The outstanding OER activity of NiCoFeO<sub>x</sub>/NF can be ascribed to the distinct crystal and electronic structure evolution as induced by the simultaneous Co and Ni incorporation: (a) the reduced nanosheet thickness and the altered crystal structure (ie, from single crystalline to poly-crystalline with the introduction of defects) increase the ECSA; (b) the electron donation from Co to Ni will make Co more acidic (Lewis

acid), which facilitates the activation of H<sub>2</sub>O (Lewis base) molecules through Lewis acid-base interaction; (c) the evolved electronic structures (the charge redistribution of the M—O bond) give rise to the promoted catalyst/electrolyte charge transfer processes and the accelerated catalysis kinetics for OER. This work not only demonstrates a facile route to better the electrocatalytic activity of TMOs catalysts, but also provides an in-depth insight into the crystal and electronic structure evolution for the enhanced OER properties.

## 4 | EXPERIMENTAL

### 4.1 | Materials

Hydrochloric acid (HCl), ethanol (C<sub>2</sub>H<sub>6</sub>O), urea (CH<sub>4</sub>N<sub>2</sub>O), ammonium fluoride (NH<sub>4</sub>F), nickel nitrate hexahydrate (Ni(NO<sub>3</sub>)<sub>2</sub>·6H<sub>2</sub>O), iron nitrate nonahydrate (Fe(NO<sub>3</sub>)<sub>3</sub>·9H<sub>2</sub>O), cobalt nitrate hexahydrate (Co(NO<sub>3</sub>)<sub>2</sub>·6H<sub>2</sub>O), and sodium hydroxide (NaOH) were purchased from Sinopharm Chemical Reagent Co., Ltd. Ni foams (NFs) were bought from Shenzhen Kejing Star Technology Co., Ltd. All chemicals were used without further purification.

### 4.2 | Hydrothermal deposition of TMOs nanosheets onto NFs

In a typical experiment, NF was cleaned with diluted HCl, ethanol, and deionized water for several times. Stoichiometric amounts of Co(NO<sub>3</sub>)<sub>2</sub>·6H<sub>2</sub>O, Ni(NO<sub>3</sub>)<sub>2</sub>·6H<sub>2</sub>O, and Fe(NO<sub>3</sub>)<sub>3</sub>·9H<sub>2</sub>O (specifically, 1 mmol of Ni(NO<sub>3</sub>)<sub>2</sub>·6H<sub>2</sub>O (or Co(NO<sub>3</sub>)<sub>2</sub>·6H<sub>2</sub>O, Fe(NO<sub>3</sub>)<sub>3</sub>·9H<sub>2</sub>O) were used to synthesize NiO<sub>x</sub> (or CoO<sub>x</sub>, FeO<sub>x</sub>); 0.5 mmol of Fe(NO<sub>3</sub>)<sub>3</sub>·9H<sub>2</sub>O and 0.5 mmol of Ni(NO<sub>3</sub>)<sub>2</sub>·6H<sub>2</sub>O (or Co(NO<sub>3</sub>)<sub>2</sub>·6H<sub>2</sub>O) were used to synthesize NiFeO<sub>x</sub> (or CoFeO<sub>x</sub>); 0.33 mmol of Co(NO<sub>3</sub>)<sub>2</sub>·6H<sub>2</sub>O, 0.33 mmol of Ni(NO<sub>3</sub>)<sub>2</sub>·6H<sub>2</sub>O, and 0.33 mmol of Fe(NO<sub>3</sub>)<sub>3</sub>·9H<sub>2</sub>O were used to synthesize NiCoFeO<sub>x</sub> were dissolved into 70 mL of deionized water to form a uniform solution, followed by addition of 1 mmol of NH<sub>4</sub>F and 2 mmol of urea with vigorous magnetic stirring. After stirring for 1 hour, the solution was transferred into the Teflon-lined autoclave, and then the pretreated NF was immersed into the reaction solution. The autoclave was sealed and maintained at 120 °C for 12 hours in an electric oven. After cooling to room temperature, the samples were collected and washed with deionized water and absolute ethanol for several times and then dried at 60 °C for 10 hours. Afterward, the samples were annealed at 400 °C for 2 hours to obtain the TMOs/NF materials.

The loading mass density of the TMOs on the NF was ≈0.1 mg cm<sup>-2</sup>.

### 4.3 | Materials characterization

Inductively coupled plasma-mass spectrometry (NexION 3500D) was applied for determining the transition metals dissolved in the electrolyte after durability test. XRD patterns were obtained from a PANalytical X'pert MPD Pro diffractometer using Ni-filtered Cu K $\alpha$  irradiation (wavelength 1.5406 Å), the voltage operated was 40 kV and the current was 40 mA. The morphology of the samples was observed through field emission scanning electron microscope (JEOL JSM-7800F) operated at 3.0 kV. High-resolution transmission electron microscopy (TEM) was carried out in a FEI Tecnai G2 F30 TEM with an accelerating voltage of 300 kV. The chemical compositions of the samples were conducted by XPS (AXIS Ultra DLD) with monochromatic Al K $\alpha$  radiation ( $h\nu = 1486.69$  eV) and with a concentric hemispherical analyzer. AFM was obtained on a Veeco NanoScope IIIA AFM instrument (Digital Instruments, Santa Barbara, California) in tapping mode. The synchrotron XASs at Fe, Co, and Ni K-edge were performed at BL17C and BL01C, at the National Synchrotron Radiation Research Center, Taiwan.

### 4.4 | Electrochemical measurements

Electrochemical measurements were performed with a potentiostat (Autolab PGSTAT302N, Metrohm) in a three-electrode cell system. TMOs/NF and commercial RuO<sub>2</sub>, a platinum plate, a saturated calomel electrode (SCE) were employed as the working electrode, counter electrode, and reference electrode, respectively. In this work, all LSVs were carried out in 1.0 M NaOH aqueous electrolyte (pH = 13.6) at a scan rate of 1 mV s<sup>-1</sup>. Furthermore, LSV were iR corrected based on the electrolyte ohmic resistance ( $R_s$ ), except the durability tests. EIS was carried out on a three-electrode cell system in 1.0 M NaOH at 25 °C, at a certain potential with sweeping frequency in the range from 100 kHz to 0.1 Hz. All potentials were calibrated to RHE using equation  $E_{\text{RHE}} = E_{\text{SCE}} + 0.244 + 0.059 \times \text{pH}$ , where  $E_{\text{RHE}}$  is the potential referred to RHE and  $E_{\text{SCE}}$  is the measured potential against SCE. The amount of O<sub>2</sub> evolved was detected by gas chromatograph (SP-2100, Beijing Beifen-Ruili Co., Ltd., China) with N<sub>2</sub> as carrier gas. The Faradaic efficiency was determined by the ratio of experimentally measured and theoretically calculated amounts of evolved O<sub>2</sub> gas during OER.

## ACKNOWLEDGMENTS

The authors gratefully acknowledge the financial support of the National Natural Science Foundation of China (No. 51961165103, 51672210). S.S. is supported by the National Program for Support of Top-notch Young Professionals.

## ORCID

Shaohua Shen  <https://orcid.org/0000-0001-8536-7386>

## REFERENCES

- Wang H-Y, Hsu Y-Y, Chen R, Chan T-S, Chen HM, Liu B. Ni<sup>3+</sup>-induced formation of active NiOOH on the spinel Ni-Co oxide surface for efficient oxygen evolution reaction. *Adv Energy Mater.* 2015;5:1500091.
- Zhu Y, Zhou W, Chen Y, Yu J, Liu M, Shao Z. A high-performance electrocatalyst for oxygen evolution reaction: LiCo<sub>0.8</sub>Fe<sub>0.2</sub>O<sub>2</sub>. *Adv Mater.* 2015;27:7150-7155.
- Dou S, Tao L, Huo J, Wang S, Dai L. Etched and doped Co<sub>9</sub>S<sub>8</sub>/graphene hybrid for oxygen electrocatalysis. *Energ Environ Sci.* 2016;9:1320-1326.
- Yang Y, Dang L, Shearer MJ, et al. Highly active trimetallic NiFeCr layered double hydroxide electrocatalysts for oxygen evolution reaction. *Adv Energy Mater.* 2018;8:1703189.
- Chai Y-M, Shang X, Liu Z-Z, et al. Ripple-like NiFeCo sulfides on nickel foam derived from in-situ sulfurization of precursor oxides as efficient anodes for water oxidation. *Appl Surf Sci.* 2018;428:370-376.
- Li P, Duan X, Kuang Y, et al. Tuning electronic structure of NiFe layered double hydroxides with vanadium doping toward high efficient electrocatalytic water oxidation. *Adv Energy Mater.* 2018;8:1703341.
- Lettenmeier P, Wang L, Golla-Schindler U, et al. Nanosized IrO<sub>x</sub>-Ir catalyst with relevant activity for anodes of proton exchange membrane electrolysis produced by a cost-effective procedure. *Angew Chem.* 2016;128:752-756.
- Wang M, Dong C-L, Huang Y-C, Shen S. Bifunctional cobalt phosphide nanoparticles with convertible surface structure for efficient electrocatalytic water splitting in alkaline solution. *J Catal.* 2019;371:262-269.
- Enman LJ, Burke MS, Batchellor AS, Boettcher SW. Effects of intentionally incorporated metal cations on the oxygen evolution electrocatalytic activity of nickel (oxy)hydroxide in alkaline media. *ACS Catal.* 2016;6:2416-2423.
- Qi J, Zhang W, Xiang R, et al. Porous nickel-iron oxide as a highly efficient electrocatalyst for oxygen evolution reaction. *Adv Sci.* 2015;2:1500199.
- Fominykh K, Chernev P, Zaharieva I, et al. Iron-doped nickel oxide nanocrystals as highly efficient electrocatalysts for alkaline water splitting. *ACS Nano.* 2015;9:5180-5188.
- Fominykh K, Feckl JM, Sicklinger J, et al. Ultrasmall dispersible crystalline nickel oxide nanoparticles as high-performance catalysts for electrochemical water splitting. *Adv Funct Mater.* 2014;24:3123-3129.
- Yan Y, Xia BY, Zhao B, Wang X. A review on noble-metal-free bifunctional heterogeneous catalysts for overall electrochemical water splitting. *J Mater Chem A.* 2016;4:17587-17603.
- Dionigi F, Strasser P. NiFe-based (oxy)hydroxide catalysts for oxygen evolution reaction in non-acidic electrolytes. *Adv Energy Mater.* 2016;6:1600621.
- Tripkovic V, Hansen HA, Vegge T. From 3D to 2D Co and Ni oxyhydroxide catalysts: elucidation of the active site and influence of doping on the oxygen evolution activity. *ACS Catal.* 2017;7:8558-8571.
- Yu JF, Wang Q, O'Hare D, Sun L. Preparation of two dimensional layered double hydroxide nanosheets and their applications. *Chem Soc Rev.* 2017;46:5950-5974.
- Zhang L, Li H, Li K, et al. Morphology-controlled fabrication of Co<sub>3</sub>O<sub>4</sub> nanostructures and their comparative catalytic activity for oxygen evolution reaction. *J Alloy Compd.* 2016;680:146-154.
- Han L, Yu X-Y, Lou XW. Formation of Prussian-blue-analog nanocages via a direct etching method and their conversion into Ni-Co-mixed oxide for enhanced oxygen evolution. *Adv Mater.* 2016;28:4601-4605.
- Wang Y, Zhang Y, Liu Z, et al. Layered double hydroxide nanosheets with multiple vacancies obtained by dry exfoliation as highly efficient oxygen evolution electrocatalysts. *Angew Chem Int Ed.* 2017;56:5867-5871.
- Qian Q, Li Y, Liu Y, Yu L, Zhang G. Ambient fast synthesis and active sites deciphering of hierarchical foam-like trimetal-organic framework nanostructures as a platform for highly efficient oxygen evolution electrocatalysis. *Adv Mater.* 2019;31:1901139.
- Xie J, Cao S, Gao L, Lei F, Hao P, Tang B. Modified bluing treatment to produce nickel-cobalt-iron spinel oxide with promoted oxygen-evolving performance. *Chem Commun.* 2019;55:9841-9844.
- Yin S, Tu W, Sheng Y, et al. A highly efficient oxygen evolution catalyst consisting of interconnected nickel-iron-layered double hydroxide and carbon nanodomains. *Adv Mater.* 2018;30:1705106.
- Liu R, Wang Y, Liu D, Zou Y, Wang S. Water-plasma-enabled exfoliation of ultrathin layered double hydroxide nanosheets with multivacancies for water oxidation. *Adv Mater.* 2017;29:1701546.
- Liu Y, Zhang M, Hu D, Li R, Hu K, Yan K. Ar plasma exfoliated ultrathin NiCo-layered double hydroxides nanosheets for enhanced oxygen evolution. *ACS Appl. Energy Mater.* 2019;2:1162-1168.
- Wang A, Zhao Z, Hu D, et al. Tuning the oxygen evolution reaction on a nickel-iron alloy via active straining. *Nanoscale.* 2019;11:426-430.
- Liang H, Meng F, Cabán-Acevedo M, et al. Hydrothermal continuous flow synthesis and exfoliation of NiCo layered double hydroxide nanosheets for enhanced oxygen evolution catalysis. *Nano Lett.* 2015;15:1421-1427.
- Tang C, Wang H-S, Wang H-F, et al. Catalysis: spatially confined hybridization of nanometer-sized NiFe hydroxides into nitrogen-doped graphene frameworks leading to superior oxygen evolution reactivity. *Adv Mater.* 2015;27:4524-4524.
- Long X, Li J, Xiao S, et al. A strongly coupled graphene and FeNi double hydroxide hybrid as an excellent electrocatalyst for the oxygen evolution reaction. *Angew Chem Int Ed.* 2014;53:7584-7588.
- Burke MS, Enman LJ, Batchellor AS, Zou S, Boettcher SW. Oxygen evolution reaction electrocatalysis on transition metal oxides and (oxy)hydroxides: activity trends and design principles. *Chem Mater.* 2015;27:7549-7558.
- Friebel D, Louie MW, Bajdich M, et al. Identification of highly active Fe sites in (Ni,Fe)OOH for electrocatalytic water splitting. *J Am Chem Soc.* 2015;137:1305-1313.

31. Li N, Bediako DK, Hadt RG, et al. Influence of iron doping on tetravalent nickel content in catalytic oxygen evolving films. *Proc Natl Acad Sci U S A*. 2017;114:1486-1491.
32. Chen Z, Cai L, Yang X, et al. Reversible structural evolution of  $\text{NiCoO}_x\text{H}_y$  during the oxygen evolution reaction and identification of the catalytically active phase. *ACS Catal*. 2018;8:1238-1247.
33. Jin Y, Shen PK. Nanoflower-like metallic conductive  $\text{MoO}_2$  as a high-performance non-precious metal electrocatalyst for the hydrogen evolution reaction. *J Mater Chem A*. 2015;3:20080-20085.
34. Hibino M, Terashima J, Yao T. Reversible and rapid discharge-charge performance of  $\gamma\text{-Fe}_2\text{O}_3$  prepared by aqueous solution method as the cathode for lithium-ion battery. *J Electrochem Soc*. 2007;154:A1107-A1111.
35. Kumar A, Bhattacharyya S. Porous NiFe-oxide nanocubes as bifunctional electrocatalysts for efficient water-splitting. *ACS Appl Mater Interfaces*. 2017;9:41906-41915.
36. Biesinger MC, Payne BP, Grosvenor AP, Lau LWM, Gerson AR, Smart RSC. Resolving surface chemical states in XPS analysis of first row transition metals, oxides and hydroxides: Cr, Mn, Fe, Co and Ni. *Appl Surf Sci*. 2011;257:2717-2730.
37. Grosvenor AP, Kobe BA, Biesinger MC, McIntyre NS. Investigation of multiplet splitting of Fe 2p XPS spectra and bonding in iron compounds. *Surf Interface Anal*. 2004;36:1564-1574.
38. Sivanantham A, Ganesan P, Shanmugam S. Bifunctional electrocatalysts: hierarchical  $\text{NiCo}_2\text{S}_4$  nanowire arrays supported on Ni foam: an efficient and durable bifunctional electrocatalyst for oxygen and hydrogen evolution reactions. *Adv Funct Mater*. 2016;26:4660-4660.
39. Chen R, Wang H-Y, Miao J, Yang H, Liu B. A flexible high-performance oxygen evolution electrode with three-dimensional  $\text{NiCo}_2\text{O}_4$  core-shell nanowires. *Nano Energy*. 2015;11:333-340.
40. Yang B, Yu L, Yan H, et al. Fabrication of urchin-like  $\text{NiCo}_2(\text{CO}_3)_{1.5}(\text{OH})_3@ \text{NiCo}_2\text{S}_4$  on Ni foam by an ion-exchange route and application to asymmetrical supercapacitors. *J Mater Chem A*. 2015;3:13308-13316.
41. Kong W, Lu C, Zhang W, Pu J, Wang Z. Homogeneous core-shell  $\text{NiCo}_2\text{S}_4$  nanostructures supported on nickel foam for supercapacitors. *J Mater Chem A*. 2015;3:12452-12460.
42. Louie MW, Bell AT. An investigation of thin-film Ni-Fe oxide catalysts for the electrochemical evolution of oxygen. *J Am Chem Soc*. 2013;135:12329-12337.
43. Trotochaud L, Young SL, Ranney J, Boettcher S. Nickel-iron oxyhydroxide oxygen-evolution electrocatalysts: the role of intentional and incidental iron incorporation. *J Am Chem Soc*. 2014;136:6744-6753.
44. Sun Y, Gao S, Lei F, Jiawei L, Liang L, Xie Y. Atomically-thin non-layered cobalt oxide porous sheets for highly efficient oxygen-evolving electrocatalysts. *Chem Sci*. 2014;5:3976-3982.
45. Qian L, Gu L, Yang L, Yuan H, Xiao D. Direct growth of  $\text{NiCo}_2\text{O}_4$  nanostructures on conductive substrates with enhanced electrocatalytic activity and stability for methanol oxidation. *Nanoscale*. 2013;5:7388-7396.
46. Xiao C, Li Y, Lu X, Zhao C. Bifunctional porous  $\text{NiFe/NiCo}_2\text{O}_4/\text{Ni}$  foam electrodes with triple hierarchy and double synergies for efficient whole cell water splitting. *Adv Funct Mater*. 2016;26:3515-3523.
47. Cheng J, Lu Y, Qiu K, et al. Hierarchical core/shell  $\text{NiCo}_2\text{O}_4@ \text{NiCo}_2\text{O}_4$  nanocactus arrays with dual-functionalities for high performance supercapacitors and Li-ion batteries. *Sci Rep*. 2015;5:12099.
48. Wang X, Yan C, Sumboja A, Lee PS. High performance porous nickel cobalt oxide nanowires for asymmetric supercapacitor. *Nano Energy*. 2014;3:119-126.
49. Zhu Y, Zhou W, Zhong Y, et al. A perovskite nanorod as bifunctional electrocatalyst for overall water splitting. *Adv Energy Mater*. 2017;7:1602122.
50. Wang M, Dong C-L, Huang Y-C, Li Y, Shen S. Electronic structure evolution in tricomponent metal phosphides with reduced activation energy for efficient electrocatalytic oxygen evolution. *Small*. 2018;14:1801756.
51. Song F, Hu X. Exfoliation of layered double hydroxides for enhanced oxygen evolution catalysis. *Nat Commun*. 2014;5:4477-4486.

## SUPPORTING INFORMATION

Additional supporting information may be found online in the Supporting Information section at the end of this article.

**How to cite this article:** Zhang X, Dong C-L, Diao Z, Lu Y-R, Shen S. Identifying the crystal and electronic structure evolution in tri-component transition metal oxide nanosheets for efficient electrocatalytic oxygen evolution. *EcoMat*. 2019;1:e12005. <https://doi.org/10.1002/eom2.12005>